scientific reports

OPEN

Microenvironments on individual sand grains enhance nitrogen loss in coastal sediments

Farooq Moin Jalaluddin[1], Soeren Ahmerkamp[1,2]✉, Hannah K. Marchant[1,3], Volker Meyer[1],
Klaus Koren[4] & Marcel M. M. Kuypers[1]

The permeable silicate sediments which cover more than 50% of the continental shelves are a major, but poorly constrained sink for the vast amount of anthropogenic nitrogen (N) that enters the ocean. Surface-attached microbial communities on sand grains remove fixed-N via denitrification, a process generally restricted to anoxic or low oxygen (O_2) environments. Yet, in sands, denitrification also occurs in the centimeters thick well-oxygenated surface layer, which leads to additional and substantial N-loss. So far however, the underlying mechanisms that drive denitrification in oxic sands are poorly resolved. In this study, we applied a non-invasive microfluidic technique to visualize and quantify how sediment-attached microorganisms shape O_2 availability on the surface of silicate sand grains. This revealed a remarkable heterogeneity in rates; with colonies of O_2 consuming and producing microorganisms situated within micrometers of each other. Using a mechanistic approach to model respiration on the surface of a single silicate sand grain we showed that the high rates of O_2 consumption within the microbial colonies on the sand-grain surface outpace O_2 supply from the surrounding pore water. As a result anoxic microenvironments develop on the sand grain surface, which so far have been invisible to conventional techniques. The model results indicate that anaerobic denitrification occurring in these anoxic microenvironments can account for up to 74% of denitrification in oxygenated sands, with the remainder occurring in the presence of oxygen. In a preliminary upscaling approach, using a global dataset we estimated that anoxic microenvironments in oxygenated surface layers could be responsible for up to a third of the total N-loss that occurs in silicate shelf sands. Consequently, denitrification in anoxic microenvironments drives substantial anthropogenic-N removal from continental silicate shelf sands.

Keywords Permeable sediments, Aerobic denitrification, Microniches, Oxic-anoxic interface, Nitrogen cycling

Permeable sands cover more than half of the continental shelf seafloor where they function as biocatalytic filters[1,2], removing vast amounts of the anthropogenically derived nitrogen (N) that reaches coastal seas via riverine and groundwater discharge[3–7]. The extensive N-loss that occurs in sands is driven by highly active sediment-attached microorganisms which are constantly re-supplied with substrates (i.e. nitrate and organic matter) due to the advective flow of seawater through the pore space between individual sand grains[5,6,8]. These microbial communities remove fixed-N from the environment via denitrification, a process which is typically restricted to anoxic or low oxygen (O_2) environments[9,10]. Yet, in sands, denitrification has been measured when O_2 concentrations within the sediment are high[7,8,11,12]. This so-called aerobic denitrification has the potential to greatly enhance the volume of sediment in which N-loss can occur, as O_2 can penetrate centimeters deep into sandy sediments dependent on pore water flow velocity[13–16]. Yet, despite the potential importance of aerobic denitrification, so far, the underlying mechanisms that drive it are still not understood.

Almost all known denitrifying microorganisms are facultative anaerobes, i.e. they can also respire O_2. However, cultured denitrifiers typically downregulate the transcription and synthesis of denitrification enzymes in the presence of O_2, as from a bioenergetic and kinetic perspective, O_2 is a more favorable electron acceptor[9]. However, in sandy sediments, microorganisms seem to constantly transcribe both aerobic and denitrification respiration

[1]Max Planck Institute for Marine Microbiology, 28359 Bremen, Germany. [2]Leibniz Institute for Baltic Sea Research Warnemünde, 18119 Rostock, Germany. [3]MARUM-Center for Marine Environmental Sciences, University of Bremen, 28359 Bremen, Germany. [4]Department of Biology, Aarhus University Centre for Water Technology, Aarhus University, Aarhus 8000, Denmark. ✉email: sahmerka@mpi-bremen.de; soeren.ahmerkamp@io-warnemuende.de

pathways as a response to the rapidly changing availability of O_2[11]. Thus, previously, aerobic denitrification in sandy sediments has been attributed to denitrifying communities performing aerobic and anaerobic respiration at the same time[8,11,17]. Additionally, the presence of anaerobic microbial activity in seemingly oxic environments can be a result of the formation of anoxic microenvironments due to biofilm formation[18,19]. When bacteria colonize surfaces in thick layers (i.e. biofilms), their respiratory activity can lead to the establishment of O_2 gradients, allowing anaerobic processes to occur even when they are surrounded by well-oxygenated waters[20–22]. This can be exacerbated in soils and sandy sediments, where the pore spaces through which water flows can be clogged by biological processes such as extensive biofilm growth[23–26], trapping of aggregates[20,27], streamers[28,29], and tortuosity effects[30,31]. However, microbial colonization on marine sand grains seems to be typically limited to monolayers of microorganisms, which are restricted to cracks and depressions on the sand grain surface[32–34]. Despite the microscale size of these sand grain surface microenvironments, diffusion limitation has still been hypothesized to occur within them[35], potentially leading to the formation of anoxic microenvironments, but so far this has never been observed. This might be a direct consequence of the fact that the techniques frequently applied to study O_2 dynamics in biofilms are unable to resolve O_2 gradients which occur within the diffusive boundary layer (DBL) surrounding single sand grain surfaces. Thus, we have been unable to gain a mechanistic understanding of how sand grain attached microorganisms shape the microenvironment around them and control the potential for anaerobic processes to occur.

Here, we visualized for the first time the microbial distribution and volumetric O_2 consumption/production rates at the surface of single silicate sand grains, using phosphorescent O_2 sensitive nanoparticles. To assess how microscale heterogeneity of O_2 consumption and production at the sand grain surface propagates into the DBL around the sand grain and the surrounding bulk pore water, we developed a multiphysics model for a silicate sand grain. Subsequently, we investigated how these micro-scale processes affect N-loss from continental silicate shelf sediments.

Results and discussion

Patchy colonization of sand grain surfaces by photo- and non-phototrophic microorganisms

We used fluorescence microscopy and SYBR Green I staining to visualize and quantify the distribution of microorganisms on the surface of single sand grains (Fig. 1A), which were collected from an intertidal region in the North Sea characterized by high microbial O_2 respiration and N-loss rates[5,6,36,37]. Microscopic imaging of cells revealed a sand surface colonization of around $1.3 \cdot 10^8$ cells cm^{-3} ($\pm 0.4 \cdot 10^8$ cells cm^{-3}) of sediment, which occurred in patches of thin monolayers (Fig. 1A, Table. S1). Although our visualization revealed that microorganisms tended to colonize the sand grain surface in patches, they also showed that microorganisms did not form the 3D-structured thick biofilms that are known to cause diffusion limitation[18–20], pore-space clogging[24] and the formation of large anoxic microniches.

To distinguish between potential photosynthetic and non-photosynthetic O_2-respiring microorganisms on the sand surface we imaged the autofluorescence (exc.: 469/35 nm, em.: > 590 nm) from chlorophyll-*a* containing microorganisms, i.e. microphytobenthos[38,39] (Fig. 1B). Correlative imaging with SYBR Green I staining showed that individual sand grains were diversely co-colonized by primary producers and other non-chlorophyll containing, likely O_2 respiring organisms (Fig. 1C). Overall, cell numbers of photosynthetic microorganisms were substantially lower than those of non-photosynthetic microorganisms ($3.5 \cdot 10^6$ cells cm^{-3} of sediment compared to a total of $1.3 \cdot 10^8$ cells cm^{-3} of sediment). These cell counts of non-photosynthetic organisms compare well to those determined previously in sandy sediments[40–43].

The morphology of the autofluorescent photosynthetic microorganisms indicated that they were likely cyanobacteria with typical sizes of < 1 µm as well as coccoid and disc-shaped diatoms which were approx. 80 µm large. These results fit to metagenomic analyses of the microbial community composition of photosynthetic microorganisms associated with intertidal sediments from the North Sea (Fig. S3). Based on the classification of small subunit (SSU) ribosomal RNA genes within the sand flat metagenome, Cyanobacteria (predominantly from the orders *Cyanobacteriales* and *Synechococcales*) comprised ~ 2% of the total bacterial community. Diatoms, particularly from the classes *Bacillariophyceae* and *Mediophyceae* comprised more than 96% of the reads associated with photosynthetic eukaryotes (Fig. S3 B). The presence of these firmly attached phototrophic microorganisms indicates that the sand grains were regularly exposed to light in situ, likely due to sediment redistribution and bedform migration[13], as light only penetrates the top few millimeters of silicate sands[44]. This dynamic environment not only supports phototrophs but also shapes a diverse microbial community in which denitrification is not confined to a single taxonomic group. Instead, the capacity for denitrification appears to be a widely shared functional trait selected for across the community[11]. Thus, we did not visualize individual taxa attached to the sand grains (as in[34]). However, the analysis of the abundance of denitrification genes relative to a housekeeping gene (*rpoB*) within the sediment, indicated that around 15–20% of the microbial community within the sediments has the potential to denitrify (Fig. S4). Taken together the microscopic imaging showed a highly heterogeneous colonization on the surface of individual sand surfaces.

Co-occurring O_2 consumption and production on individual sand grains

The sand grains were collected from an intertidal flat in a region which is characterized by high net O_2 respiration and N-loss rates (e.g[36,37]). In line with this, we observed a similar high net O_2 consumption as previous studies (~ 26 µmol O_2 L^{-1} h^{-1}[45]). To determine the O_2-respiration by individual surface-attached microbial colonies, we developed a new microfluidic-based imaging method (Fig. 1D). Briefly, we coated sand grains with phosphorescent O_2-sensitive nanoparticles and subsequently quantified the change in O_2 concentrations over time. We carried out the experiments under low light conditions in order to quantify the impact of both the photo- and non-phototrophic organisms on the sand grains. We observed heterogeneities in O_2 concentrations developing at the surface of individual sand grains within 30 min, with patches on the sand grain surfaces

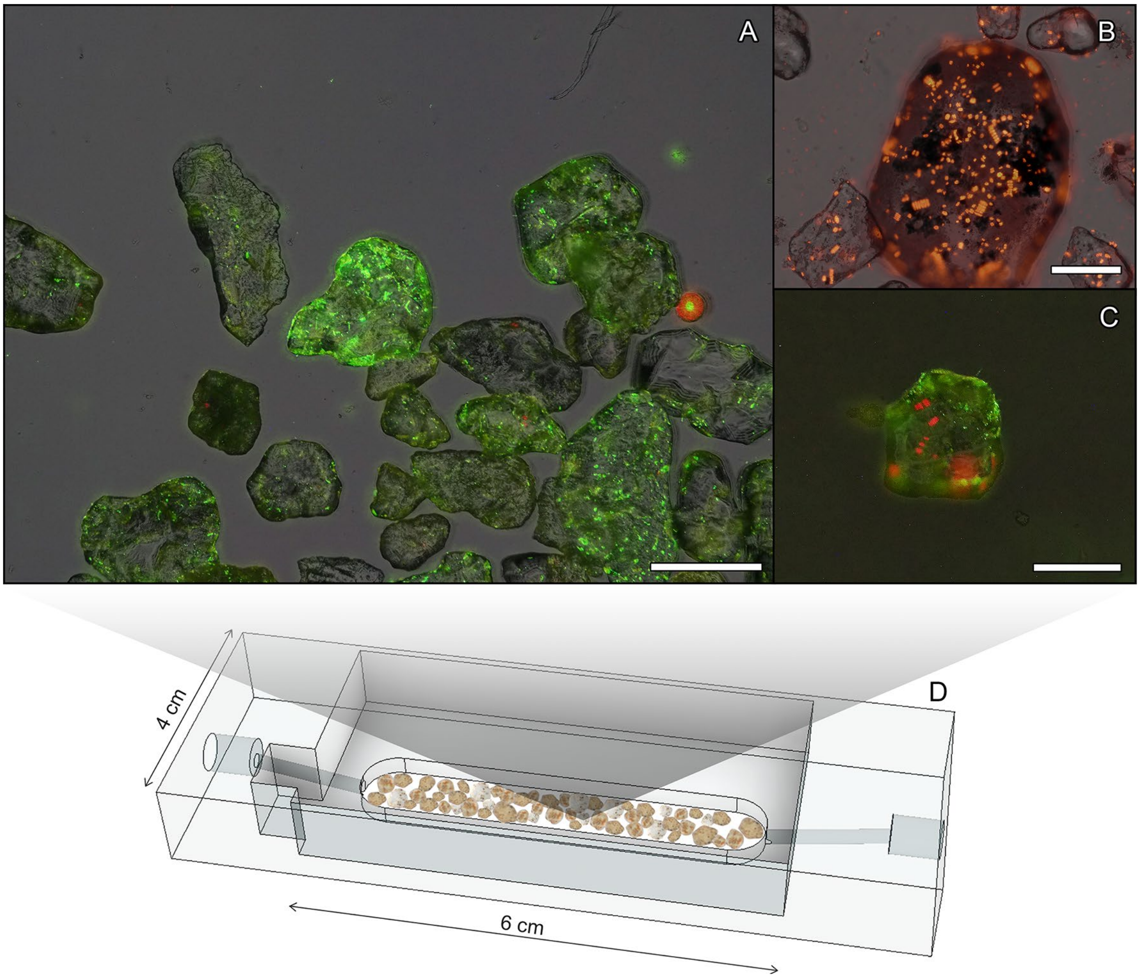

Fig. 1. Micrographs showing the colonization of single sand grains by microorganisms. (**A**) dsDNA staining (SYBR Green I, green, exc.:469/35 nm, em.: 510/42 nm) overlaid with RGB image of sand grains revealing the heterogeneous microbial colonization on individual sand grains, (**B**) autofluorescence image (red) showing colonization of chlorophyll-*a* containing phototrophic microorganisms (exc.: 469/35 nm, em.: > 590 nm), (**C**) overlay of dsDNA staining (green) and autofluorescence image (red) reveals co-colonization of photo- and non-phototrophic microorganisms on the sand grains. (**D**) Conceptual view of the acrylic microfluidic device filled with sand grains to conduct the incubations. See also Table S1. Scalebars denote 250 µm.

turning anoxic within one hour; even though O_2 concentrations were still > 100 µmol O_2 L^{-1} on adjacent parts of the sand grain (Fig. 2A and Fig. S5). Until now, these anoxic microenvironments on the surface of silicate sand grains escaped detection because they are too small to resolve using more conventional instruments like microsensors[46,47]. Imaged changes in O_2 concentration were used to determine volumetric O_2 production and consumption rates on micrometer scales (1–10 µm) (see methods for details). Net median volumetric O_2 rates were approx. -20 µmol O_2 L^{-1} h^{-1} but varied strongly from -46 µmol O_2 L^{-1} h^{-1} (25% percentile) to 12 µmol O_2 L^{-1} h^{-1} (75% percentile) (Fig. 2). Overall, our direct imaging approach revealed a mosaic of O_2 consuming and producing patches situated within micrometers of each other on the surface of a single sand grain (Fig. 2B-D).

The patches of O_2 production directly correlated to areas colonized by auto-fluorescent phototrophic O_2-producing microorganisms, while the O_2-consuming areas were non-fluorescent, most likely representing colonies of non-photosynthetic O_2 respiring microorganisms (Fig. 2E). Both these functional groups of microorganisms are known to colonize sand grains[48–51], however their ability to noticeably affect O_2 gradients over such small scales has not been reported before. The chlorophyll-*a* containing photosynthetic patches had median O_2 production rates of 19 µmol O_2 L^{-1} h^{-1} (Fig. 2E, red). Whereas the regions without chlorophyll-a had a net O_2 consumption rate of 26 µmol O_2 L^{-1} h^{-1} (Fig. 2E, blue). The decrease in O_2 concentration for the entire incubation time period (4 h) was non-linear, most likely caused by diffusion limitations (see Fig. S6). However, the net consumption values represent a conservative estimate due to non-linear decrease and as we observed O_2 consumption in some of the masked areas containing primary producers.

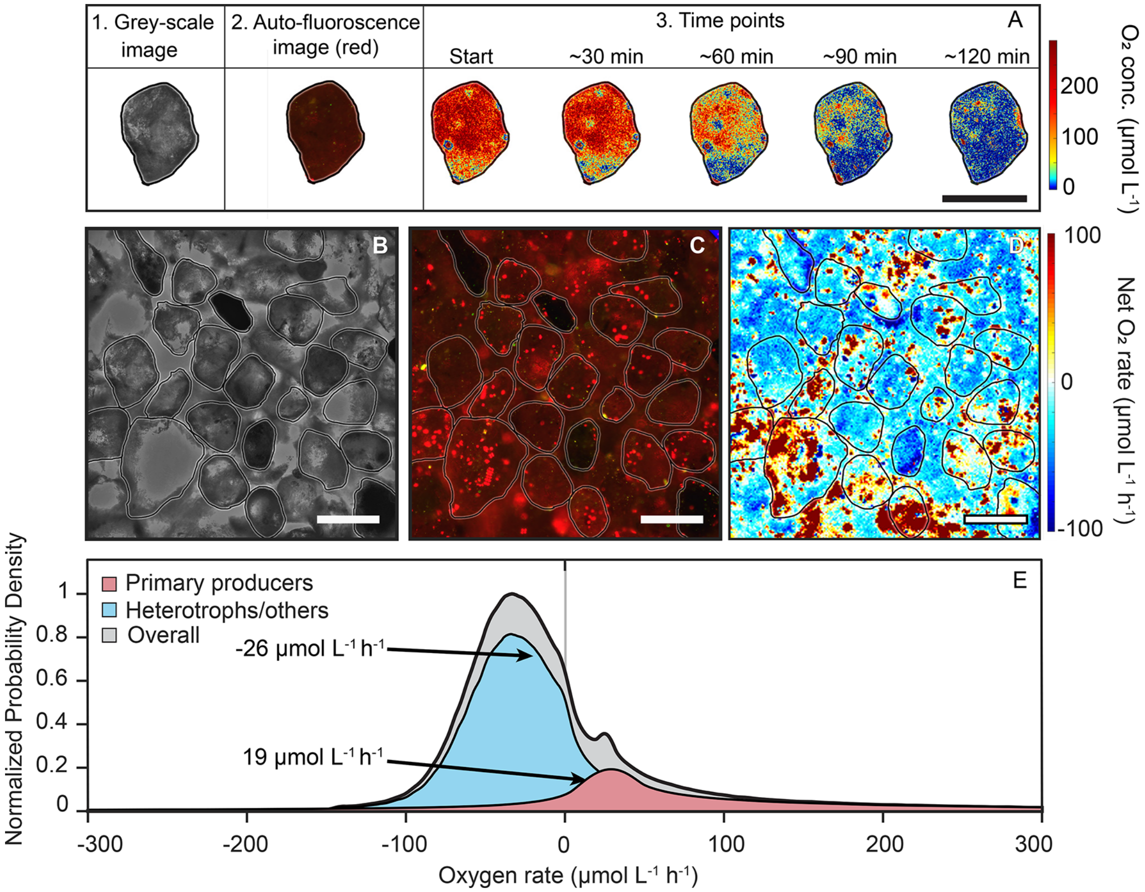

Fig. 2. Microbial colonization of silicate sand grain surfaces and associated zones of O_2 production and consumption that result in highly heterogeneous O_2 concentrations at the surface of sand grains. (**A**) Development of heterogenous O_2 concentrations on the surface of single sand grain over time. A.1 grey scale image of a sand grain. A.2 Auto-fluorescence (exc.: 469/35 nm, em.: > 590 nm) as an indicator for oxygen-producing photosynthetic microorganisms. A.3 Heterogeneities in O_2 concentrations developing over time at the sand grain surface. (**B**) Grey-scale image of silicate sand grains incubated within the microfluidic chip, (**C**) auto-fluorescence image (exc.: 469/35 nm, em.: > 590 nm) showing the location of photosynthetic microorganisms on the sand grain surfaces, (**D**) O_2 consumption and production on the sand grain surface in the microfluidic chip (blue color indicates O_2 consumption rate and red color indicates O_2 production rate. (**B**–**D**) The same field of view. (**E**) Normalized density distribution of the O_2 rate for microenvironments, depicted in grey. The O_2 rates were subsequently classified based on whether photosynthetic microorganisms were present in the pixels where the rate was measured, with net production highlighted in red, and other microenvironments showing net consumption, indicated in blue. Arrows indicate the median O_2 rates of 19 µmol L^{-1} h^{-1} and -26 µmol L^{-1} h^{-1} for the photosynthetic microorganisms and other microorganisms, respectively. Note that the O_2 consumption could have been associated with heterotrophic remineralization of organic matter as well as chemolithotrophic processes such as nitrification. Scalebars denote 200 µm.

Mechanism leading to anoxic microenvironments and denitrification on single sand grains

We derived a multiphysics model for a typical silicate sand grain (median diameter 290 µm, Fig. 3, Fig. S7) to assess how heterogeneity of O_2 consumption and production at the sand grain surface propagates into the diffusive boundary layer (DBL) around the sand grain and the surrounding bulk pore water. First, we used the volumetric O_2 consumption and production rates determined using the microfluidic-chip to model the O_2 consumption/production rate heterogeneity at the sand grain surface (see methods). The O_2 consumption and production rates on the microbially colonized surface of the sand grain were modeled to range between -955 mmol L^{-1} h^{-1} and 514 mmol L^{-1} h^{-1}, corresponding to single cell O_2-respiration and photosynthesis rates of 0.4 fmol O_2 cell^{-1} h^{-1} and 7.1 fmol O_2 cell^{-1} h^{-1}, respectively (see methods). Subsequently, microbial colonies with net O_2 production and consumption rates were distributed across the modelled sand grain surface (Fig. 3A), simulating the observed patchy distribution of microbial colonies, respiration and photosynthesis (Figs. 1 and 2). Finally, we varied pore water velocities and bulk O_2 concentrations in the model to assess how O_2 consumption/production rate heterogeneity at the sand grain surface propagates into the DBL and surrounding bulk pore water in the presence of pore water flow. A total of 1764 model runs, with pore water O_2 concentrations from 1 to 100 µmol L^{-1} and pore water flow velocities of 0 to 500 µm s^{-1} were carried out to simulate the ranges observed in the environment[13,52–54] (see Table S1 for summary of all parameters). The sand grain model results revealed

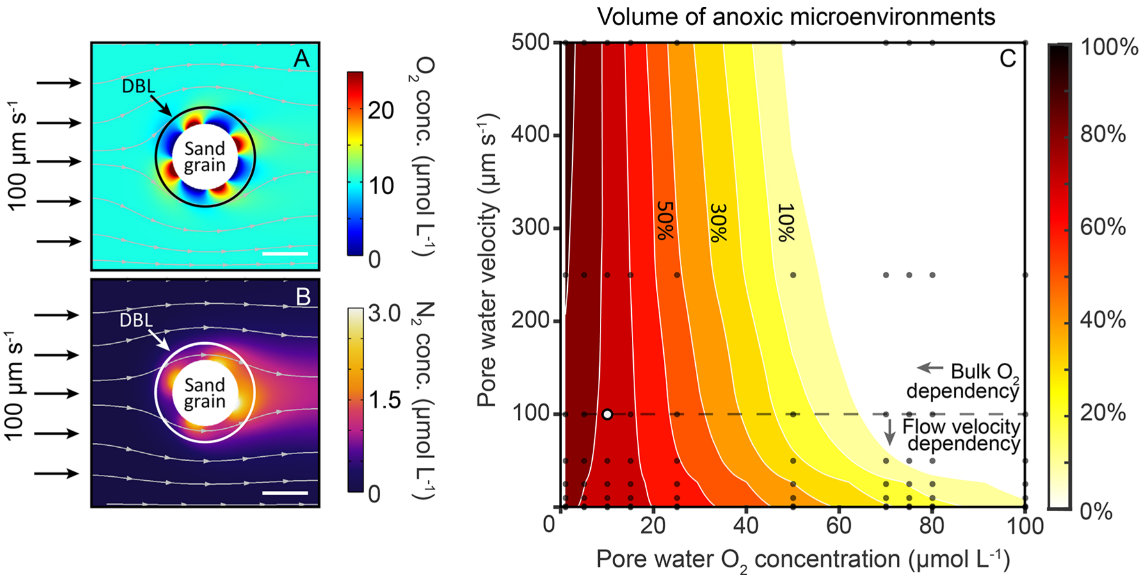

Fig. 3. The development of anoxic microenvironments and associated N-loss on a modelled sand grain colonized with O_2 consuming and producing microbial colonies. (**A**) Patchy distribution of oxygen (O_2) producing and consuming microenvironments within the diffusive boundary layer (DBL) indicate the fast cycling of O_2 on micrometer scales and the formation of anoxic microenvironments on the sand surface, despite the presence of bulk ambient O_2. (**B**) Even though zones of production and consumption are in direct proximity, anoxic microenvironments are formed in the presence of O_2 resulting in the production of nitrogen (N_2) through denitrification. Streamlines indicate the flow field (scale bar in (**A**), (**B**) represents 200 µm). (**C**) Phase diagram indicating the anoxic volume (in which rates are taking place) in dependence to pore water velocities and inflow O_2 concentrations (based on 80 model runs indicated through gray dots, white dot indicates model run depicted in (**A**), (**B**)). At lower flow velocities (below 10 µm s^{-1}), the volume of anoxic microenvironments is strongly dependent on the flow velocities through which the boundary layer thickness (diffusive length scale) is determined. At higher flow velocities (above 100 µm s^{-1}) the anoxic volumes mainly depend on inflow O_2 concentrations. An additional 80 model runs were carried out where no O_2 production was occurring to simulate a scenario with no photosynthetic activity, and showed similar results (Fig. S9 and supporting information text).

that the variations in O_2 concentrations resulting from O_2 rate heterogeneity at the sand surface propagated into the DBL, but not into the surrounding pore water (Fig. 3A). Consequently, the DBL around individual sand grains had O_2 concentrations which differed greatly from the surrounding pore waters, even when the pore waters were well ventilated. Furthermore, the modelling runs indicated that between 20 and 100% of the net O_2-respiring non-photosynthetic microbial colonies on the sand grain surface turn anoxic when pore water O_2 concentrations were below 50 µmol L^{-1} or when pore water velocities were lower than 100 µm s^{-1} (Fig. 3C). Under these conditions anoxic microenvironments formed as respiration rates outpaced the diffusion of O_2 into the DBL (Fig. 3C). Intriguingly, we found that the activity of photosynthetic microbial colonies on the sand grain surface had only a minor effect on the volume of anoxic microenvironments, implying that the results are also applicable to non-illuminated silicate sandy sediments (see methods and supplementary information text). Sand grain surface roughness was not included in the main modeling results or sensitivity analysis, which makes our estimates on microenvironments conservative. To evaluate its potential effect, we conducted additional calculations in which surface roughness, represented as height deviations from a smooth surface was tested for its impact on DBL thickness at flow velocities between 10 and 100 µm s^{-1} (see methods). This revealed that surface roughness, which was between ~2–35 µm could increase the DBL thickness by up to 20%. Such an increase would reduce diffusive exchange between the grain surface and surrounding pore water, thereby promoting the formation of anoxic microsites.

Subsequently, having identified when microbial colonies turn anoxic, we included a denitrification parametrization within the single sand grain model, using the ratio of denitrification rates to O_2 consumption rates determined previously for sandy shelf sediments (Fig. S8, see methods). This robust empirical correlation between O_2 consumption rates and denitrification rates under oxic and anoxic conditions, respectively, is derived from diverse sandy sediment studies[5,12,17,35,55,56], and is a well-established proxy by which denitrification is determined in benthic modelling studies (e.g[57]. By applying this parameterization, we observed substantial N_2 production at the surface of the sand grains with rates of 0.2 nmol N per day per anoxic microbial colony, summing to a total of 0.8 nmol N per day per sand grain, which diffused from the DBL into the porewater (Fig. 3B).

Overall, the model reproduced the observed microbial colonization and O_2 dynamics of a single sand grain, and showed that, anoxic microenvironments form due to O_2 consumption rates at the sand grain surface outpacing diffusive O_2 supply from the surrounding oxic pore water (Fig. 3A). We confirmed that the development of

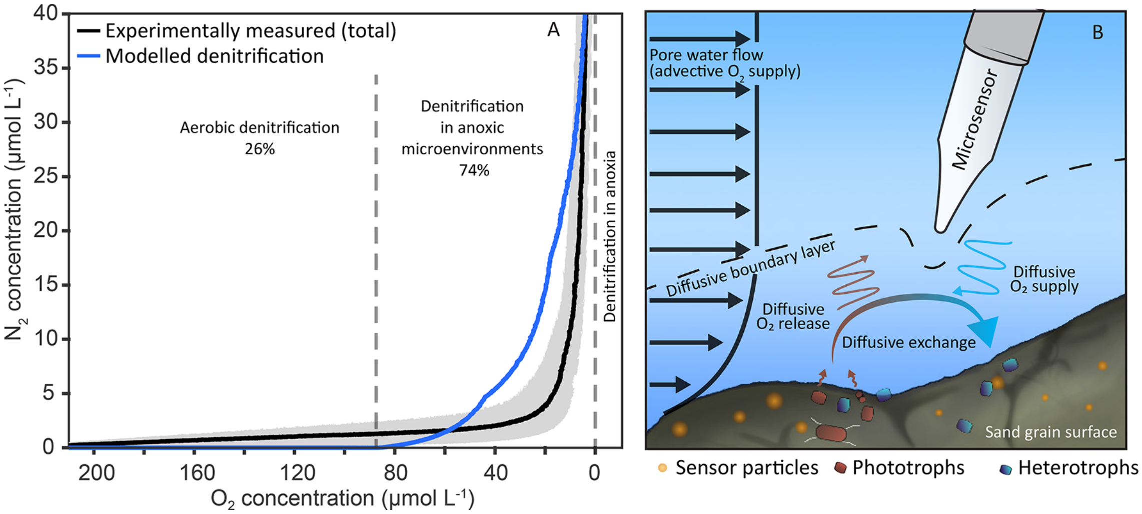

Fig. 4. Modelled N_2 production from anaerobic denitrification in anoxic microenvironments compared to experimental observations of N_2 production in the presence of O_2. (**A**) The relationships derived from the modeling outputs were applied to a previously published dataset[11] where N_2 production was measured simultaneously to oxygen respiration in sandy sediments (mean concentration as solid line and gray shaded area represents the concentration range from different experiments). This allowed an estimation of the proportion of sand grain surfaces which were anoxic for the given oxygen concentration; subsequently N_2 production was calculated within these microenvironments based on the maximal anoxic rate of denitrification measured in the same incubation (blue solid line). Anoxic microenvironments started accumulating within the sediment even when bulk pore water still had an O_2 concentration of 90 µmol L^{-1}. The remaining N_2 production could not be attributed to anoxic microenvironments and was likely produced in the presence of oxygen (data used can be found in Fig. S10). Based on the model relationships, aerobic denitrification contributes 26%, while denitrification in anoxic microenvironments accounts for 74% of denitrification under oxic conditions. (**B**) Reduction of porewater velocity around sand grains leads to a limited supply of substrate due to the formation of a diffusive boundary layer (DBL). When microbial respiration rates within the boundary layer exceed diffusion of O_2 into the DBL, local spots of anoxia can form, even when O_2 is produced nearby by O_2 producing microorganisms. Conventional techniques such as micro-sensors would not be able to resolve these micrometer scale patches of anoxia as they disrupt the DBL which leads to mixing between the anoxic and oxic microenvironments as well as the surrounding waters.

anoxic microenvironments is a persistent feature in a total of 1764 model runs where O_2 consumption rates in the microbial colonies, diffusion coefficients, flow velocity and microbial distributions were varied. It is likely that this mechanism of anoxic microsite formation is active throughout the oxic silicate sands of the continental shelves, as they are all exposed to similar physical forcing and flow conditions[2] and furthermore, exhibit similar microbial communities[9,51,58–60] and microbial colonization patterns[32,34,48].

The role of anoxic microenvironments in biogeochemical cycling in oxic sandy shelf sediments

The diffusive O_2 supply through the DBL and the volumetric O_2 consumption/production rate at the sand grain surface from the single sand grain model were used to derive a power-law relationship that can predict the volume of anoxic microenvironments in a given volume of sandy sediment (Fig. S9 and supporting information text). To validate the relationship, we compared the outcomes to experimentally derived denitrification rates which were observed in the presence of O_2 in sandy sediments from the North Sea[11]. When O_2 consumption rates, grain sizes and flow velocities from the experiment were used as input parameters, the relationship predicted N_2 production in anoxic microenvironments to start when pore water O_2 concentrations dropped below ~ 90 µmol O_2 L^{-1} (Fig. 4A). The N_2-concentration increased exponentially until O_2 dropped to zero, which is in good agreement with the exponential N_2 production observed experimentally. Overall, the relationship could explain around 74% of the total N_2 production that was experimentally observed under oxic conditions (220 to 1 µmol O_2 L^{-1}; Fig. 4A and Fig. S10). The other 26% of experimentally determined N_2 production occurred when pore water O_2 concentrations were above 90 µmol O_2 L^{-1}, where the relationship predicted that anoxic environments would not yet have started to form. This implies that the low, but linear rates observed under high O_2 concentrations (above 90 µmol O_2 L^{-1}) are likely derived from microorganisms carrying out denitrification in the presence of O_2 i.e. so-called aerobic denitrification[8,11,61].

The power-law relationship was then integrated into a reaction-transport model developed to predict solute (e.g. O_2 and nitrate) exchange fluxes in permeable sandy sediments[5,13,62]. The modified reaction-transport model revealed that by neglecting anaerobic denitrification in anoxic microenvironments, the N_2-fluxes from sandy sediments in the German Bight (North Sea) were underestimated by ~ 33% in our previous study[5]. Subsequently, we tested whether anaerobic denitrification in anoxic microenvironments has the potential to contribute to total

N_2 fluxes in other silicate shelf sediments, where O_2 rates, sand grain size and bottom water velocities differ significantly from the German Bight. We used previously published data from six globally distributed sand sites as input parameters for our modified reaction transport model[4,6,7,11,12,61]. These sites represent a broad range of shelf ecosystems including; coastal upwelling off North-West Africa, a sandy beach seepage face (Sangguo bay, China), a temperate coastal sea (North Sea); a shallow subtropical ocean basin (Gulf of Mexico), a temperate coastal ocean (the South Atlantic bight) and shallow coastal sediments in Australia. All sites were characterized by silicate sands with grain sizes ranging from 102 to 700 µm, bottom water velocities between 0.1 and 0.2 m s^{-1} and denitrification rates from 0.04 to 11.8 µmol N L^{-1} h^{-1}.

Despite the large variations in measured environmental conditions and estimated volumetric rates, the upscaling approach indicated that anaerobic denitrification within anoxic microenvironments in oxic sands always contributed substantially to the total denitrification and ranged between 8 and 62% (average 33%; Table S2). The largest source of uncertainty in these estimates is the scaling from the measured bulk rates to the volumetric rates within microbial colonies on sand grains (see supplementary information text). To account for this uncertainty, we varied the estimated volumetric rates in microbial colonies by ± 50%, resulting in an error margin ranging from 4 to 22% (see methods, supplementary information text, and Fig. S14). Our findings imply that anaerobic denitrification in anoxic microenvironments is likely responsible for the previously observed denitrification in oxic sands[6–8,11,17].

Although our results may not be directly transferable to the ~ 20% of sandy shelf sediments dominated by carbonate sands[63] or to impermeable sandy sediments (see limitations in the supplementary information text) they indicate that anaerobic microbial activity within anoxic microenvironments is a substantial driver of the N-loss via denitrification that has previously been experimentally observed within the oxic zone of silicate sandy sediments (Fig. 4A, Table S2). The close proximity of oxic and anoxic microenvironments on the surface of silicate sand grains likely also plays a role in the strong coupling of nitrification and denitrification in sandy sediments[5]. Likewise, the presence of anoxic microenvironments might enhance spatial overlaps between other processes such as sulfide oxidation and sulfate reduction[64,65] as well as influence the mobilization and redistribution of iron and manganese-oxides in silicate sands[36,66,67,68].

The discovery of anoxic microenvironments on the surface of individual sand grains reveals a heretofore-unknown mechanism that allows anaerobic microbial activity to occur in environments where O_2 is rapidly replenished by advective pore water flow (Fig. 4B). Our combined results indicate that anaerobic denitrification in these anoxic microenvironments is a substantial sink for anthropogenic-N entering the oceans and thus plays a key role in marine biogeochemical nitrogen cycling.

Materials and methods

Sample collection

Sediment samples and sea water for the incubations were collected from an intertidal flat in Dorum, North Sea (53.64° N, 8.49° E) in January 2021. A spatula was used to collect the benthic surface sediment (top 1 cm), collected in a pre-washed plastic transport box, and transferred to the lab in Bremen in a cool box. Sediment was stored immersed in sea water in the dark at 12 °C on shaker and sub-samples were collected for the incubations.

Microbial colonization and cell counting on sand grains

Silicate sand grains were incubated for 15 min in the dark with SYBR Green I (1:10,000 dilution in DMSO). Subsequently the sediment was washed twice with phosphate-buffered saline (PBS). SYBR Green I stains all the microorganisms containing dsDNA (double-stranded DNA) and is used to visualize the colonization of microorganisms on the sand grain surface. Subsequently, sand grains were placed in a frame (10 × 10 mm; created using transparent tape) on standard glass slides. Fluorescent microscopes (Olympus microscope BX53 and Zeiss Axio Imager M2) were used to image green fluorescence (exc.: 469/35 nm, em.: 510/42 nm) from stained dsDNA and chlorophyll-*a* auto-fluorescence (exc.: 469/35 nm, em.: > 590 nm). The chlorophyll-*a* auto-fluorescence was used to distinguish photosynthetic microorganisms from other organisms[69,70]. Staining and fluorescence z-stack images were used for cell counting on a total 50 sand grains (Fig. 1, S1 and S2). Regions of interest (ROI) were chosen randomly on the sand grain surfaces for counting the number of cells per area.

Subsequently, the cell numbers per sediment volume were calculated by multiplying the cells per area (average $8.57 \cdot 10^5$ cells $cm^{-2} \pm 2.8 \cdot 10^5$ cells cm^{-2}) with the surface-to-volume ratio (Eq. 1). For this, we first determined the grain size distribution from images of the collected sand grains ($n \sim 400$, Fig. S11). The images were processed in Matlab (R2019a, Mathworks) to determine diameters (d_g, Fig. S11). The porosity (θ, ratio of void volume and total volume) was estimated by preparing 10 ml of water saturated sediment, which was left overnight in the oven to dry (Fraser, 1935). From the weight difference the void volume was used to calculate the porosity of 0.4. The surface to volume ratio ($S_{V,\,T}$) of the sediments was then calculated based on the measured grain size distribution using:

$$S_{V,T} = 6\,(1 - \theta\,) \int_{d_2}^{d_1} \frac{p\,(d_g)}{d_g} \mathrm{d}d_g \tag{1}$$

where $p(d_g)$ is the probability density function of the respective sediment fractions and d_g the diameter of the grains. The average surface to volume ratio in our case was calculated to be 153 cm^2 cm^{-3} resulting in average cell numbers of $1.3 \cdot 10^8$ cells cm^{-3} of sediment.

Metagenomic analysis of photosynthetic and denitrifying communities

A previously published metagenome[64] was reanalyzed to investigate the photosynthetic community composition and relative abundance of denitrification genes. The photosynthetic microbial community composition based on SSU rRNA gene sequences in the metagenome was determined using phyloFlash v3.4.1[71], using the previously outlined approach[72]. Briefly, 16S and 18S rRNA reads were mapped onto reference databases using phyloFlash[71]. For 18S rRNA based analysis, the PR2 version 5.0.0 database was used[73]. For 16S rRNA, a database was created using all bacterial and archaeal entries of the SILVA SSU database version 138[74] together with the PhytoREF chloroplast 16S rRNA database[75]. Reads assigned to chloroplasts in the 18S rRNA analysis were removed.

To estimate the abundance of denitrifying genes, trimmed reads from the metagenomes were compared against the custom gene reference databases using DIAMOND v2.0.15[76]. To remove false positives, protein sequences from all genomes of species representatives in the genome taxonomy database (GTDB) version R207[77] and the genomic catalog of Earth's microbiomes[78] were used as the outgroup of the genes. The identified reads were searched against the outgroup using DIAMOND v2.0.15 with the same parameters. Reads meeting the following requirements were considered: (1) the match score of the read against the gene reference database > = 100 and (2) the ratio of the match score against the gene database divided by the match score against the outgroup > = 0.9. The read coverage of denitrification genes was normalized by the gene length and the read coverage of the beta subunit of RNA polymerase, RpoB. The obtained fraction represents the estimated proportion of denitrifying microorganisms in the metagenomes, assuming a single gene copy per organism.

Sensor particle fabrication

Sensor particles were prepared by precipitation as described earlier[79–82]. The sensor particles consist of two dyes, namely, platinum(II)-5,10,15,20-tetrakis-(2,3,4,5,6-penta- fluorophenyl)-porphyrin (PtTFPP; exci.: ~400 nm or ~ 540 nm, em.: ~650 nm) and macrolex fluorescent yellow 10GN (MY; exc.: ~450 nm, em.: ~480 nm). The former is an oxygen (O_2) dependent dye and the latter is a reference dye to compensate for bleaching of sensor particles and an inhomogeneous illumination[83,84]. Further, MY acts as an antenna dye which allows for the excitation of both dyes with a wavelength of 450 nm. The stock solution of sensor particles was centrifuged for two minutes (Eppendorf centrifuge 5430R) and the supernatant was replaced with collected seawater, this was repeated three times. For calibration, the sensor particle solution was filled in a 6 ml glass vial (Exetainer, LabCo, UK) and O_2 concentration in the solution was controlled by degassing with N_2 gas and air (21% O_2). The O_2 concentration was monitored using needle optodes (Pyroscience). Correlation between the ratiometric signal and O_2 concentrations was established using the curve fitting tool in Matlab (see Fig. S12).

Volumetric O_2 consumption rate estimates using sensor particles

An acrylic microfluidic chip was designed in which sand grains were coated with sensor particles and incubations were performed (chamber dimensions 35 × 7.8 × 2 mm, Fig. 1D). A thin layer (~ 600 µm) of sand was gently spread out in the chamber of the microfluidic chip using a sterile lab spatula and 1 ml of the prepared sensor particle solution was injected into the chip from the top using a syringe. The added solution was slowly removed from the chip using 1 ml syringes attached at the outlets. This procedure was repeated three times resulting in a homogenous coating of the sediments with sensor particles, keeping the pore space free from sensor particles. The outlets were sealed and the chip was filled with filtered (0.2 µm) seawater, targeting sediment-attached microorganism based on studies indicating that 95 – 99% of microorganisms in silicate continental shelf sediments are found on sand grains rather than in the porewater[43,85,86]. The top of the microfluidic chip was covered using a glass coverslip. The incubation was performed under low light conditions of around 0.4 µmol photons m^2 s^{-1}, which is in the lower range of light reaching intertidal or subtidal shelf systems (e.g[44,87,88]. Although we could not measure the light directly within the chip it is likely that the light levels within the chip were higher due to increased irradiance (caused due to small and confined space)[89].

The prepared microfluidic chip was mounted on an inverted microscope (Leica DMI 6000B) with a sCMOS camera attached (pco.panda 4.2). An LED light source (Omicron LedHUB® – High-Power LED Light Engine) with a wavelength of 455 nm and output power 2400 mW was used for excitation. Images were recorded through the bottom glass with an exposure of ~ 200 ms and stored using the pco.camware 4.11 software. A polyester filter (Lee filter-101 Yellow; emi.: >480 nm) was applied to ensure that only emissions from the sensor particles were recorded. During the incubation, images were captured approximately every 20–30 min until no substantial changes were observed, i.e. the microfluidic chip turned anoxic. RGB images were captured at a resolution of 2048 × 2048 pixels. After incubations, the density of sensor particles was quantified from scanning electron micrographs as 5 particles per µm² (Fig. S13 A-B). Additionally, lifetime imaging using a pco.1600 camera (Excelitas PCO AG) attached to a custom-made modulator for light source triggering was used to capture lifetime images from the sensor particles. The lifetime imaging confirmed the homogeneous distribution of the sensor particles (Fig. S13 C-D).

All post-processing was carried out using Matlab (R2019a, Mathworks). A ratiometric imaging approach was used to estimate the volumetric O_2 consumption and production rates in the acquired RGB images. For each time point 10 images were captured and averaged, the raw images were split into red and green channels and the ratio was calculated:

$$Ratio = \frac{Red\ channel\ \ (indicator\ dye)}{Green\ channel\ \ (reference\ dye)} \tag{2}$$

The ratio is related to the specific O_2 concentration through the Stern-Volmer equation (see Fig. S12). The O_2 production and consumption rates from the microfluidic incubation were calculated by estimating the pixel wise differences of the ratio for two time points in the chip, divided by the incubation time:

$$R = \frac{f\left(Ratio_{t1}\right) - f\left(Ratio_{t0}\right)}{t} \tag{3}$$

R is the O_2 rate (µmol O_2 L^{-1} h^{-1}), $Ratio_{t1}$ is ratiometric values at time t_1, $Ratio_{t0}$ is the ratiometric values at time t_0, t is incubation time in hours (t_1 - t_0). In the approach, we assume that at t_0, the O_2 concentration is homogeneously distributed around the sand grain. The O_2 respiration rates calculated using this approach for the entire incubation period of four hours are rather a conservative estimate, due to no-flow in the microfluidic chip causing diffusion limitations. For processing of the O_2 rate matrix, a threshold was set to remove outliers, and data was smoothed using the medfilt2 function with a 5 × 5 kernel. O_2 rates were masked through thresholding based on the chlorophyll-*a* auto-fluorescence. Thereby, net consuming microbial colonies are separated from net producing microbial colonies for subsequent quantifications. Note that in some cases O_2 production was observed in areas containing non-autofluorescent microorganisms. These regions were not abundant and are likely due to the integration of emission signals from the sand grains due to their 3D structure and reflections.

Modeling single sand grains and the formation of microenvironments

To investigate the effect of the patchy microbial colonization on a single sand grain under varying environmental conditions, we developed a two-dimensional multiphysics model (Comsol multiphysics 5.6). The model domain consists of circular sand grain with a reactive domain (5 µm) on the sand surface (Fig. S7). The flow field is calculated by solving the laminar Stokes equations:

$$0 = -\nabla \mathrm{p} + \mu \nabla^2 \boldsymbol{u} \tag{4}$$

$$\nabla \cdot \boldsymbol{u} = 0 \tag{5}$$

u is the velocity vector, p the pressure, µ dynamic viscosity (1.22·10^{-3} Pa·s) and ∇ the gradient-operator.

The oxygen (O_2) and dinitrogen (N_2) distribution was calculated by solving the stationary advection-diffusion equations:

$$0 = D \nabla^2 C_{O2,N2} - \boldsymbol{u} \cdot \nabla C_{O2,N2} - R_c \tag{6}$$

D is diffusion coefficient (1.1·10^{-9} m^2 s^{-1} for O_2, and 2.1·10^{-9} m^2 s^{-1} for N_2 at 25 °C corrected for EPS in the colonization patches[19], ∇ the gradient-operator, C_{O2} is concentration of O_2 and C_{N2} the concentration of N_2, **u** is the velocity vector. No-flux, slip boundary conditions were applied at the top, and bottom boundaries and no-slip boundary conditions on the sand grain boundary (see Fig. S7). Inlet and outlet boundaries as inflow and outflow for the assigned pore water flow. For R_c, we applied a sinusoidal function along the surface of the sand grain to produce alternating patterns of production and consumption in a 5 µm thin layer:

$$R_{c=} \left(R_{O2,N2}\right) \cdot \left(\sin\left(\operatorname{atan}\left(\frac{y}{x}\right) \cdot a\right)\right) \cdot f_{O2,N2}(\mathrm{C}) \tag{7}$$

Where y and x are the spatial coordinates. $R_{O2,\, N2}$ are the volumetric O_2 consumption rates within microbial colonies at the sand grain surface. These colonies and their associated O_2 consumption rate occur in 1/1000 of the entire pore volume. To determine $R_{O2,\, N2}$, we used our measured O_2 consumption rates that represent the volumetric rate of the entire pore volume. To convert the measured rate from the entire pore volume to the microbial colonies, we divided the 25th percentile of measured rates (-46 µmol O_2 L^{-1} h^{-1}) by the cell numbers of 1.3 ·10^8 cells cm^{-3} to estimate the cell-specific rate of -0.4 fmol O_2 $cell^{-1}$ h^{-1}. Subsequently we divided the cell-specific rate by their characteristic biovolume (0.4 µm^3 which yields the rate of the microbial colonies of R_{O2} = -955 mmol O_2 L^{-1} h^{-1}. Phototrophic microorganisms sparsely colonized the surfaces of sand grains, resulting in O_2 production occurring on approximately one-third of the sand grain surfaces, while O_2 consumption takes place on approximately two-thirds of the sand grain surfaces (Fig. 2D). To take this into account, the sinus curve (R_c) was shifted downwards, so that the final colony sizes are 76 µm for the net O_2 consuming microbial colonies and 38 µm for the net O_2 producing microbial colonies. Four consuming and four producing colonies were modelled along the sand grain (a = 4). The final minima of R_c are at $R_{c,\, min}$ = -955 mmol O_2 L^{-1} h^{-1} representing net-consuming colonies and the maxima of R_c are at $R_{c,\, max}$= 514 mmol O_2 L^{-1} h^{-1} representing net producing colonies. When considering the lower cell numbers of 3.5 ·10^6 cells cm^{-3} of phototrophic organisms the net producing colony values correspond to 7.1 fmol O_2 $cell^{-1}$ h^{-1}. Employing this approach, we assume that within the microbial colonies, the volumetric rates follow a normal distribution, gradually decreasing from the core towards the outer regions.

Further, for the consumption of O_2, we incorporated a Michaelis-Menten kinetic: $f_{O2}(C) = C_{O2}/(K_m + C_{O2})$, where C_{O2} is the concentration of O_2, K_m is the half-saturation coefficient of the O_2 consumption rate (K_m = 0.1 µmol L^{-1}). The production of N through denitrification was set proportional to the volumetric O_2 consumption rate at a ratio of 10:1, which is based on empirical observations (See Fig. S14) with an inhibition constant of N at C_{inh} = 0.1 µmol L^{-1}. The inhibition was incorporated through the function $f_N(C) = C_{inh}/(C_{inh} + C_{O2})$ (see also[90].

We first performed 160 model runs, of which, 80 runs involved the direct application of Eq. 7, with variations in porewater velocities ranging from 0 to 500 µm s^{-1} and pore water O_2 concentrations ranging from 0 to 100 µmol L^{-1}. Subsequently, a second round of model runs was conducted in which values within the reactive domain with R_c > 0 were set to zero. The parametrization for porewater velocities and pore water O_2 concentrations was adjusted to the same values as in the first run with consumption and production. To evaluate the sensitivity of the parameters utilized in the model, we ran in total 1764 model runs expanding the range of applied parameters to conditions typically present in other sandy sediments of other regions (see supplementary information text).

Estimation of the sand grain roughness

To quantify sand grain surface roughness and evaluate its impact on the diffusive boundary layer (DBL), we followed an approach based on Yao & Li (2023)[91], adapted to a 2D framework using microscopic images. High-resolution images of individual sand grains ($n \approx 40$) were analyzed to extract their outlines, which were then compared to their respective convex hulls (Fig. S16). Surface roughness (in micrometers) was calculated as the radial difference between the actual grain outline and its convex hull, providing a geometric measure of the surface irregularity. The processing was performed in Matlab R2019b (Mathworks).

Relationships for the development of anoxic microenvironments

To incorporate our model results into a previously published reaction-transport model, we derived a non-dimensional number: "Sand_{DBL}". The Sand_{DBL} number represents the ratio of diffusive exchange of O_2 into the boundary layer and the activity of the microbial colonies. First, the diffusive boundary layer thickness δ around a single sand grain was estimated by applying a previously derived scaling law[92,93]:

$$\delta = \frac{r}{Sh} \tag{8}$$

where r is median radius of the sediments, Sh is Sherwood number $\text{Sh} = 1 + 0.62 \cdot \text{Re}^{0.41}\,\text{Sc}^{0.33}$, Re is Reynolds number $\text{Re} = \text{U}r/\nu$, U is pore water velocity, ν is kinetic viscosity, Sc is Schmidt number $\text{Sc} = \nu/\text{D}$, D is diffusion coefficient of O_2 in water. The Sand_{DBL} number (analog to the Damköhler number) is then calculated by estimating the diffusive time scale to the reaction time scale:

$$\text{Sand}_{\text{DBL}} = \frac{\delta^2}{D} \cdot \frac{R_{O2}}{C_0} \tag{9}$$

where R_{O2} is reaction rate, C_0 is bulk O_2 concentrations. We found that for $\text{Sand}_{\text{DBL}} < 10$ microbial colonies on the sand grain are mostly oxic and for $\text{Sand}_{\text{DBL}} > 1000$ the microbial colonies are mostly anoxic. For the intermediate range $10 < \text{Sand}_{\text{DBL}} < 1000$ we estimated the best fit between anoxic volumes of the microbial colonies and the Sand_{DBL} (for additional details see supplementary information text). A total of 1764 model runs were used for the determine the relationship between the Sand_{DBL} number and the volume of anoxic microenvironments (Supp. Equation 1 and Supp. Equation 2).

Areal denitrification estimates

We used a model approach to estimate the contribution of denitrification within anoxic microenvironments to total denitrification based on field-obtained data. The model allows an effective mixing depth D in sandy sediments to be calculated as a function of time t[5,13,62]:

$$D = \frac{1}{k\,\ln\left(\frac{0.42\,k^2 K\,h_m t}{\theta} + 1\right)} \tag{10}$$

Where h_m is the hydraulic head (m), θ the porosity, k the wavenumber λ/(2·pi), λ the characteristic bedform size, K is the hydraulic conductivity (m s^{-1}). The bedform size is determined following the empirical relationship $\lambda = 490 \cdot d_g$[13]. The hydraulic head follows $h_m = 1000 \cdot U^2 \cdot 0.1/10000$, where U is the bottom water velocity (as in[94]. The hydraulic conductivity is calculated as $K = P / \nu \cdot g$, where P is the permeability which can be determined by the grain size: $p = 9.869 \cdot 10^{-13} \cdot 735 \cdot d_g^{2} \cdot 1e^{-6}$[95], ν is the temperature-dependent kinematic viscosity and g the acceleration by gravity. To determine the characteristic pore water velocity U, we used the equation $U = k \cdot K \cdot h_m$[62]. To take anoxic microenvironments into account, we calculated the O_2 penetration depths by estimating the time until O_2 is depleted: $t = c_{O2} / R$, where c_{O2} is the temperature dependent bottom water concentration of O_2. This timescale t is then used in Eq. 10. Subsequently, we mathematically split the oxic sediment into four layers and in each of these layers we calculated the Sand_{DBL} number to determine the volume of anoxic microenvironments (Supp. Equation 3). We then multiplied the volume of anoxic microenvironments with the volumetric denitrification rate. Integrating the resulting values over the O_2 penetration depth yields the denitrification flux in anoxic microenvironments. To determine denitrification fluxes from the anoxic sediment, we calculated the nitrate penetration depth by calculating the time until nitrate is depleted and by using this time in Eq. 10. Finally, we integrated the volumetric denitrification rate over the nitrate penetration depth to estimate the denitrification flux below the oxic-anoxic interface.

For the parametrization we compiled a dataset with globally distributed grain sizes, O_2 respiration rates, denitrification rates, bottom water velocities, bottom water O_2 concentrations and bottom water nitrate concentrations (Table S2). For the implementation of the parameterization to field data from other published studies, we used the reported O_2 bottom water concentrations and temperatures from the respective publications and adjusted for temperature-dependent solubility, diffusion coefficients, and kinematic viscosity accordingly. In case if the specific data was not provided in the publications, we calculated O_2 solubility based on the study site's temperature and salinity. Additionally, the O_2 diffusion coefficient, which is temperature-dependent, was adjusted according to the temperature values reported in the respective publications by the authors. When using this dataset for the parameterization, we found the contribution of denitrification in anoxic microenvironments to range between 8 and 62%. Sensitivity testing of key parameters influencing Sand_{DBL} and the power-law for prediction of anoxic microenvironments revealed that the volumetric rates within microbial colonies were the most sensitive parameter. In our upscaling approach, we estimated these volumetric rates on sand grain surfaces by scaling them relative to the bulk volumetric rates reported by the authors. We accounted for the uncertainty of this approach by varying the resulting volumetric rates within microbial colonies by +- 50%. The resulting range is provided as the uncertainty in the estimated contributions of anoxic microenvironments to total denitrification (see Table S2). The Matlab (R2019a, Mathworks) script for the calculations can be found on github (https://github.com/SoerenAhmerkamp/SandDBL).

Data availability

The MATLAB (R2019a, MathWorks) code and the COMSOL Multiphysics 5.6 model is available online at https://github.com/SoerenAhmerkamp/SandDBL. All measurement data are included within the manuscript or provided in the Supplementary Material.

Received: 15 January 2025; Accepted: 30 April 2025

References

1. Boudreau, B. P. et al. Permeable marine sediments: overturning an old paradigm. *Eos (Washington DC)*. **82**, 133–136 (2001).
2. Huettel, M., Berg, P. & Kostka, J. E. Benthic exchange and biogeochemical cycling in permeable sediments. *Ann. Rev. Mar. Sci.* **6**, 23–51 (2014).
3. Chua, E. J., Huettel, M., Fennel, K. & Fulweiler, R. W. A case for addressing the unresolved role of permeable shelf sediments in ocean denitrification. *Limnol. Oceanogr. Lett.* **7**, 11–25 (2022).
4. Gihring, T. M., Lavik, G., Kuypers, M. M. M. & Kostka, J. E. Direct determination of nitrogen cycling rates and pathways in Arctic Fjord sediments (Svalbard, Norway). *Limnol. Oceanogr.* **55**, 740–752 (2010).
5. Marchant, H. K. et al. Coupled nitrification-denitrification leads to extensive N loss in subtidal permeable sediments. *Limnol. Oceanogr.* **61**, 1033–1048 (2016).
6. Sokoll, S. et al. Extensive nitrogen loss from permeable sediments off North-West Africa. *J. Geophys. Res. Biogeosci*. **121**, 1144–1157 (2016).
7. Jiang, S. et al. Response of nitrate processing to bio-labile dissolved organic matter supply under variable oxygen conditions in a sandy beach seepage face. *Front. Mar. Sci.* **8**, (2021).
8. Gao, H. et al. Aerobic denitrification in permeable Wadden sea sediments. *ISME J.* **4**, 417–426 (2010).
9. Chen, J. & Strous, M. Denitrification and aerobic respiration, hybrid electron transport chains and co-evolution. *Biochim. Biophys. Acta Bioenerg*. **1827**, 136–144 (2013).
10. Zumft, W. G. Cell biology and molecular basis of denitrification. *Microbiol. Microbiol. Mol. Biology Reviews* 61 (1997).
11. Marchant, H. K. et al. Denitrifying community in coastal sediments performs aerobic and anaerobic respiration simultaneously. *ISME J.* **11**, 1799–1812 (2017).
12. Evrard, V., Glud, R. N. & Cook, P. L. M. The kinetics of denitrification in permeable sediments. *Biogeochemistry* **113**, 563–572 (2013).
13. Ahmerkamp, S. et al. Regulation of benthic oxygen fluxes in permeable sediments of the coastal ocean. *Limnol. Oceanogr.* **62**, 1935–1954 (2017).
14. Huettel, M., Røy, H., Precht, E. & Ehrenhauss, S. Hydrodynamical impact on biogeochemical processes in aquatic sediments. *Hydrobiologia* **494** (2003).
15. Huettel, M. & Gust, G. Solute release mechanisms from confined sediment cores in stirred benthic chambers and flume flows. *Mar. Ecol. Prog Ser.* **82**, 187–197 (1992).
16. Precht, E. & Huettel, M. Rapid wave-driven advective pore water exchange in a permeable coastal sediment. *J. Sea Res.* **51**, 93–107 (2004).
17. Rao, A. M. F., McCarthy, M. J., Gardner, W. S. & Jahnke, R. A. Respiration and denitrification in permeable continental shelf deposits on the South Atlantic Bight: N2:Ar and isotope pairing measurements in sediment column experiments. *Cont. Shelf Res.* **28**, 602–613 (2008).
18. Costerton, J. Overview of microbial biofilms. *J. Ind. Microbiol.* **15**, 137–140 (1995).
19. Stewart, P. S. Diffusion in biofilms. *J. Bacteriol.* **185**, 1485–1491 (2003).
20. Ceriotti, G., Borisov, S. M., Berg, J. S. & De Anna, P. Morphology and size of bacterial colonies control anoxic microenvironment formation in porous media. *Environ. Sci. Technol.* **56**, 17471–17480 (2022).
21. Ploug, H., Kühl, M., Buchholz-Cleven, B. & Jørgensen, B. Anoxic aggregates - an ephemeral phenomenon in the pelagic environment? *Aquat. Microb. Ecol.* **13**, 285–294 (1997).
22. Stewart, P. S. & Franklin, M. J. Physiological heterogeneity in biofilms. *Nat. Rev. Microbiol.* **6**, 199–210 (2008).
23. Jørgensen, B. B. Bacterial sulfate reduction within reduced microniches of oxidized marine sediments. *Mar. Biol.* **41**, 7–17 (1977).
24. Coyte, K. Z., Tabuteau, H., Gaffney, E. A., Foster, K. R. & Durham, W. M. Microbial competition in porous environments can select against rapid biofilm growth. *Proc. Natl. Acad. Sci.* **114**, E161–E170 (2017).
25. Aufrecht, J. A. et al. Pore-scale hydrodynamics influence the Spatial evolution of bacterial biofilms in a microfluidic porous network. *PLoS One*. **14**, e0218316 (2019).
26. Kurz, D. L. et al. Competition between growth and shear stress drives intermittency in preferential flow paths in porous medium biofilms. *Proc. Natl. Acad. Sci.* 119, (2022).
27. Lehto, N., Glud, R. N., á Nordi, G., Zhang, H. & Davison, W. Anoxic microniches in marine sediments induced by aggregate settlement: biogeochemical dynamics and implications. *Biogeochemistry* **119**, 307–327 (2014).
28. Drescher, K., Shen, Y., Bassler, B. L. & Stone, H. A. Biofilm streamers cause catastrophic disruption of flow with consequences for environmental and medical systems. *Proc. Natl. Acad. Sci. U S A*. **110**, 4345–4350 (2013).
29. Scheidweiler, D., Peter, H., Pramateftaki, P., de Anna, P. & Battin, T. J. Unraveling the biophysical underpinnings to the success of multispecies biofilms in porous environments. *ISME J.* **13**, 1700–1710 (2019).
30. Franklin, S., Vasilas, B. & Jin, Y. More than Meets the dye: evaluating Preferential flow paths as microbial hotspots. *Vadose Zone J.* **18**, 1–8 (2019).
31. Matyka, M., Khalili, A. & Koza, Z. Tortuosity-porosity relation in porous media flow. *Phys. Rev. E Stat. Nonlin Soft Matter Phys.* **78**, (2008).
32. Anderson, J. G. & Meadows, P. S. Microenvironments in marine sediments. *Proceedings of the Royal Society of Edinburgh. Section B. Biological Sciences* 76, 1–16 (1978).
33. Miller, D. Abrasion effects on microbes in sandy sediments. *Mar. Ecol. Prog Ser.* **55**, 73–82 (1989).
34. Probandt, D., Eickhorst, T., Ellrott, A., Amann, R. & Knittel, K. Microbial life on a sand grain: from bulk sediment to single grains. *ISME J.* **12**, 623–633 (2018).

35. Ahmerkamp, S. et al. The effect of sediment grain properties and Porewater flow on microbial abundance and respiration in permeable sediments. *Sci. Rep.* **10**, (2020).
36. de Beer, D. et al. Transport and mineralization rates in North sea sandy intertidal sediments, Sylt-Rømø basin, Wadden sea. *Limnol. Oceanogr.* **50**, 113–127 (2005).
37. Gao, H. et al. Intensive and extensive nitrogen loss from intertidal permeable sediments of the Wadden sea. *Limnol. Oceanogr.* **57**, 185–198 (2012).
38. Nelson, J. R., Eckman, J. E., Robertson, C. Y., Marinelli, R. L. & Jahnke, R. A. Benthic microalgal biomass and irradiance at the sea floor on the continental shelf of the South Atlantic Bight: Spatial and Temporal variability and storm effects. *Cont. Shelf Res.* **19**, (1999).
39. Kühl, M. & Polerecky, L. Functional and structural imaging of phototrophic microbial communities and symbioses. *Aquat. Microb. Ecol.* **53**, 99–118 (2008).
40. Dale, N. G. Bacteria in intertidal sediments: factors related to their distribution. *Limnol. Oceanogr.* **19**, 509–518 (1974).
41. Llobet-Brossa, E., Ramon, R. M. & Amann, R. Microbial community composition of Wadden sea sediments as revealed by fluorescence in situ hybridization. *Appl. Env Microbiol.* **64** (1998).
42. Meyer-Reil, L. A., Dawson, R., Liebezeit, G. & Tiedge, H. Fluctuations and interactions of bacterial activity in sandy beach sediments and overlying waters. *Mar. Biol.* **48** (1978).
43. Rusch, A., Forster, S. & Huettel, M. Bacteria, diatoms and detritus in an intertidal sandflat subject to advective transport across the water-sediment interface. *Biogeochemistry* **55** (2001).
44. Thoral, F., Pinkerton, M. H., Tait, L. W. & Schiel, D. R. Spectral light quality on the seabed matters for macroalgal community composition at the extremities of light limitation. *Limnol. Oceanogr.* **68**, 902–916 (2023).
45. Polerecky, L., Franke, U., Werner, U., Grunwald, B. & De Beer, D. High Spatial resolution measurement of oxygen consumption rates in permeable sediments. *Limnol. Oceanogr. Methods*. **3**, 75–85 (2005).
46. Revsbech, N. P. & Jørgensen, B. B. Microelectrodes: their use in microbial ecology. *Adv. Microb. Ecol.* **9** (1986).
47. Glud, R. N., Gundersen, J. K., Jorgensen, B. B., Revsbech, N. P. & Schulz, H. D. Diffusive and total oxygen uptake of deep-sea sediments in the Eastern South Atlantic Ocean: in situ and laboratory measurements. *Deep-Sea Res.* **1** (1994).
48. Kuriyama, K., Gründling-Pfaff, S., Diehl, N., Woelfel, J. & Karsten, U. Microphytobenthic primary production on exposed coastal sandy sediments of the Southern Baltic sea using ex situ sediment cores and oxygen optodes. *Oceanologia* **63**, 247–260 (2021).
49. Paterson, D. M. Biogenic structure of early sediment fabric visualized by low-temperature scanning electron microscopy. *J. Geol. Soc.* **152** (1995).
50. Zetsche, E., Paterson, D. M., Lumsdon, D. G. & Witte, U. Temporal variation in the sediment permeability of an intertidal sandflat. *Mar. Ecol. Prog Ser.* **441**, 49–63 (2011).
51. Mills, H. J. et al. Characterization of nitrifying, denitrifying, and overall bacterial communities in permeable marine sediments of the Northeastern Gulf of Mexico. *Appl. Environ. Microbiol.* **74**, 4440–4453 (2008).
52. Reimers, C. E. et al. In situ measurements of advective solute transport in permeable shelf sands. *Cont. Shelf Res.* **24**, 183–201 (2004).
53. Savant, S. A., Reible, D. D. & Thibodeaux, L. J. Convective transport within stable river sediments. *Water Resour. Res.* **23**, 1763–1768 (1987).
54. Wörman, A. Analytical solution and timescale for transport of reacting solutes in rivers and streams. *Water Resour. Res.* **34**, 2703–2716 (1998).
55. Marchant, H. K., Lavik, G., Holtappels, M. & Kuypers, M. M. M. The fate of nitrate in intertidal permeable sediments. *PLoS One* **9**, (2014).
56. Santos, I. R., Eyre, B. D. & Glud, R. N. Influence of Porewater advection on denitrification in carbonate sands: evidence from repacked sediment column experiments. *Geochim. Cosmochim. Acta*. **96**, 247–258 (2012).
57. Fennel, K. et al. Nitrogen cycling in the middle Atlantic Bight: results from a three-dimensional model and implications for the North Atlantic nitrogen budget. *Global Biogeochem. Cycles* **20**, (2006).
58. Probandt, D. et al. Permeability shapes bacterial communities in Sublittoral surface sediments. *Environ. Microbiol.* **19**, 1584–1599 (2017).
59. Kessler, A. J. et al. Bacterial fermentation and respiration processes are uncoupled in anoxic permeable sediments. *Nat. Microbiol.* **4**, 1014–1023 (2019).
60. Miksch, S. et al. Bacterial communities in temperate and Polar coastal sands are seasonally stable. *ISME Commun.* **1**, (2021).
61. Rao, A. M. F., McCarthy, M. J., Gardner, W. S. & Jahnke, R. A. Respiration and denitrification in permeable continental shelf deposits on the South Atlantic Bight: rates of carbon and nitrogen cycling from sediment column experiments. *Cont. Shelf Res.* **27**, 1801–1819 (2007).
62. Elliott, A. H. & Brooks, N. H. Transfer of nonsorbing solutes to a streambed with bed forms: theory. *Water Resour. Res.* **33**, 123–136 (1997).
63. Hayes, M. O. Relationship between coastal climate and bottom sediment type on the inner continental shelf. *Mar. Geol.* **5**, 111–132 (1967).
64. Dyksma, S., Pjevac, P., Ovanesov, K. & Mussmann, M. Evidence for H2 consumption by uncultured Desulfobacterales in coastal sediments. *Environ. Microbiol.* **20**, 450–461 (2018).
65. Bourceau, O. M. et al. Simultaneous sulfate and nitrate reduction in coastal sediments. *ISME Commun.* **3**, (2023).
66. Keiluweit, M., Gee, K., Denney, A. & Fendorf, S. Anoxic microsites in upland soils dominantly controlled by clay content. *Soil. Biol. Biochem.* **118**, 42–50 (2018).
67. Védère, C., Vieublé Gonod, L., Nunan, N. & Chenu, C. Opportunities and limits in imaging microorganisms and their activities in soil microhabitats. *Soil Biol. Biochem.* **174** (2022).
68. Zhou, Z., Henkel, S., Kasten, S., Holtappels, M.: The iron "redox battery" in sandy sediments: Its impact on organic matter remineralization and phosphorus cycling. *Sci Total Enviro*, **865**, https://doi.org/10.1016/j.scitotenv.2022.161168.
69. Franqueira, D., Orosa, M., Torres, E., Herrero, C. & Cid, A. Potential use of flow cytometry in toxicity studies with microalgae. *Sci. Total Environ.* **247** (2000).
70. Greg Mitchell, B. & Kiefer, D. A. Chlorophyll α specific absorption and fluorescence excitation spectra for light-limited phytoplankton. *Deep Sea Res. Part. Oceanogr. Res. Papers*. **35**, 639–663 (1988).
71. Gruber-Vodicka, H. R., Seah, B. K. B. & Pruesse, E. phyloFlash: Rapid Small-Subunit rRNA Profiling and Targeted Assembly from Metagenomes. *mSystems* 5, (2020).
72. Duerschlag, J. et al. Niche partitioning by photosynthetic plankton as a driver of CO2-fixation across the oligotrophic South Pacific subtropical ocean. *ISME J.* **16**, 465–476 (2022).
73. Guillou, L. et al. The protist ribosomal reference database (PR2): A catalog of unicellular eukaryote small Sub-Unit rRNA sequences with curated taxonomy. *Nucleic Acids Res.* **41**, (2013).
74. Quast, C. et al. The SILVA ribosomal RNA gene database project: improved data processing and web-based tools. *Nucleic Acids Res.* **41**, (2013).
75. Decelle, J. et al. PhytoREF: A reference database of the plastidial 16S rRNA gene of photosynthetic eukaryotes with curated taxonomy. *Mol. Ecol. Resour.* **15**, 1435–1445 (2015).
76. Buchfink, B., Xie, C. & Huson, D. H. Fast and sensitive protein alignment using DIAMOND. *Nat. Methods*. **12**, 59–60 (2014).

77. Parks, D. H. et al. An ongoing census of bacterial and archaeal diversity through a phylogenetically consistent, rank normalized and complete genome-based taxonomy. *Nucleic Acids Res. 50*. **GTDB**, D785–D794 (2022).
78. Nayfach, S. et al. A genomic catalog of Earth's microbiomes. *Nat. Biotechnol.* **39**, 499–509 (2021).
79. Ahmerkamp, S. et al. Simultaneous visualization of flow fields and oxygen concentrations to unravel transport and metabolic processes in biological systems. *Cell. Rep. Methods* **2**, (2022).
80. Koren, K., Brodersen, K. E., Jakobsen, S. L. & Kühl, M. Optical sensor nanoparticles in artificial sediments-a new tool to visualize O2 dynamics around the rhizome and roots of seagrasses. *Environ. Sci. Technol.* **49**, 2286–2292 (2015).
81. Koren, K., Jakobsen, S. L. & Kühl, M. In-vivo imaging of O2 dynamics on coral surfaces spray-painted with sensor nanoparticles. *Sens. Actuators B Chem.* **237**, 1095–1101 (2016).
82. Mistlberger, G. et al. Multifunctional magnetic optical sensor particles with tunable sizes for monitoring metabolic parameters and as a basis for nanotherapeutics. *Adv. Funct. Mater.* **20**, 1842–1851 (2010).
83. Li, C. et al. Planar optode: A two-dimensional imaging technique for studying spatial-temporal dynamics of solutes in sediment and soil. *Earth Sci. Rev.* **197** (2019).
84. Moßhammer, M., Brodersen, K. E., Kühl, M. & Koren, K. Nanoparticle- and microparticle-based luminescence imaging of chemical species and temperature in aquatic systems: a review. *Microchim. Acta* **186** (2019).
85. Mendoza-Lera, C. et al. Importance of advective mass transfer and sediment surface area for streambed microbial communities. *Freshw. Biol.* **62**, 133–145 (2017).
86. Musat, N. et al. Microbial community structure of sandy intertidal sediments in the North sea, Sylt-Rømø basin, Wadden sea. *Syst. Appl. Microbiol.* **29**, 333–348 (2006).
87. Cahoon, L. The Role of Benthic Microalgae in Neritic Ecosystems Primary Production in the Surf Zone *Oceanography and Marine Biology* (1999).
88. Barnett, A., Méléder, V., Dupuy, C. & Lavaud, J. The vertical migratory rhythm of intertidal microphytobenthos in sediment depends on the light photoperiod, intensity, and spectrum: evidence for a positive effect of blue wavelengths. *Front. Mar. Sci.* **7**, (2020).
89. Kuhl, M., Lassen, C. & Jorgensen, B. B. Light penetration and light intensity in sandy marine sediments measured with irradiance and scalar irradiance fiber-optic microprobes. *Mar. Ecol. Prog Ser.* **105**, 139–148 (1994).
90. Kessler, A. J., Cardenas, M. B., Santos, I. R. & Cook, P. L. M. Enhancement of denitrification in permeable carbonate sediment due to intra-granular porosity: A multi-scale modelling analysis. *Geochim. Cosmochim. Acta.* **141**, 440–453 (2014).
91. Yao, T. & Li, W. Quantifying the particle shape and surface roughness of sands. *Bull. Eng. Geol. Environ.* **82**, (2023).
92. Kiørboe, T. Formation and fate of marine snow: small-scale processes with large- scale implications. *Sci. Mar.* **65**, 57–71 (2001).
93. Ploug, H., Hietanen, S. & Kuparinen, J. Diffusion and advection within and around sinking, porous diatom aggregates. *Limnol. Oceanogr.* **47**, 1129–1136 (2002).
94. Ahmerkamp, S., Winter, C., Janssen, F., Kuypers, M. M. M. & Holtappels, M. The impact of bedform migration on benthic oxygen fluxes. *J. Geophys. Res. Biogeosci.* **120**, 2229–2242 (2015).
95. Gangi, A. F. Variation of whole and fractured porous rock permeability with confining pressure. *Int. J. Rock. Mech. Min. Sci. Geomech. Abstracts.* **15**, 249–257 (1978).

Acknowledgements

We thank D. Tienken, G. Klockgether, S. Littmann, P. Färber, O. Artmann, and F. Schramm for technical assistance; T. Ferdelman and M. Holtappels for sample logistics; S. Li for metagenomic analyses; G. Lavik, A. Chennu, J. Milucka, J. von Arx, A. Kidane and F. Lange for fruitful discussions. H.K.M. and F.M.J. received funding from the DFG under Germany's Excellence Strategy (no. EXC-2077-390741603). S.A. and K.K. acknowledge funding by Novo Nordisk Fonden (Grant No. 0079370) and S.A. acknowledges funding from Leibniz-Association (Strategic Institute Expansion: "Shallow Water Processes and Transitions to the Baltic Scale"). The research was funded by the Max Planck Society.

Author contributions

F.M.J., S.A. and M.M.M.K. designed the research; F.M.J performed the experiments; F.M.J. and S.A., designed the chip, and developed the model; F.M.J. and S.A. analysed, and visualized data; V.M., developed the lifetime imaging modulation box; K.K. provided sensor-particles; F.M.J., S.A., H.K.M. and M.M.M.K. wrote the paper with contributions from all co-authors.

Funding

Open Access funding enabled and organized by Projekt DEAL.

Declarations

Competing interests

The authors declare no competing interests.

Additional information

Supplementary Information The online version contains supplementary material available at https://doi.org/10.1038/s41598-025-00755-3.

Correspondence and requests for materials should be addressed to S.A.